

Heterointerface Control over Lithium-induced Phase Transitions in MoS₂ Heterostructures

Joshua V. Pondick^{1,2}, Aakash Kumar^{1,2}, Mengjing Wang^{1,2}, Sajad Yazdani^{1,2}, John M. Woods^{1,2}, Diana Y. Qiu^{1,2}, Judy J. Cha^{1,2*}

¹Department of Mechanical Engineering and Materials Science, Yale University, New Haven, CT 06511, USA.

²Energy Sciences Institute, Yale West Campus, West Haven, CT 06516, USA.

*Correspondence to: judy.cha@yale.edu

Abstract

Phase transitions of two-dimensional materials and their heterostructures enable many applications including electrochemical energy storage, catalysis, and memory; however, the nucleation pathways by which these transitions proceed remain underexplored, prohibiting engineering control for these applications. Here, we demonstrate that the lithium intercalation-induced 2H-1T' phase transition in MoS₂ proceeds via nucleation of the 1T' phase at a heterointerface by monitoring the phase transition of MoS₂/graphene and MoS₂/hexagonal boron nitride (*h*BN) heterostructures with Raman spectroscopy *in situ* during intercalation. We observe that graphene-MoS₂ heterointerfaces require an increase of 0.8 V in applied electrochemical potential to nucleate the 1T' phase in MoS₂ compared to *h*BN-MoS₂ heterointerfaces. The increased nucleation barrier at graphene-MoS₂ heterointerfaces is due to the reduced charge transfer from lithium to MoS₂ at the heterointerface as lithium also dopes graphene based on *ab initio* calculations. Further, we show that the growth of the 1T' domain propagates along the heterointerface, rather than through the interior of MoS₂. Our results provide the first experimental observations of the heterogeneous nucleation and growth of intercalation-induced phase transitions in two-dimensional materials and heterointerface effects on their phase transition.

Main Text

Nucleation phenomena are fundamental to many natural processes, and remain a critical area of study in a wide range of fields including protein phase transitions in biology,¹⁻⁴ nucleation of atmospheric particulates in climate science,^{5,6} crystallization dynamics in metals for structural materials,⁷⁻⁹ and synthesis of nanomaterials.¹⁰⁻¹² Phase transitions are initiated by nucleation, and

the transition pathways between phases are complex and heavily influenced by factors such as nanoscale confinement and interfaces.¹³ For layered transition metal dichalcogenides (TMDs) that can exist in several structural polymorphs,¹⁴ the phase transitions between these polymorphs have proven important for neuromorphic memristive computing,^{15–17} catalytic production of hydrogen,^{18–22} and logic devices.²³ To effectively exploit these phase transitions for these applications, understanding the thermodynamics and kinetics of the nucleation pathways is essential; however, nucleation pathways remain virtually unexplored for many TMDs that have been demonstrated to undergo phase transitions.

For example, despite the well-established phase transition from the semiconducting 2H phase to the semimetallic 1T' phase via lithium intercalation into the TMD MoS₂,^{24–27} the nucleation pathway has not been experimentally studied at the microscopic level. *Ab initio* calculations indicate that the lithium-induced phase transition in MoS₂ is due to the electron doping from intercalated lithium atoms into the conduction band of 2H-MoS₂: at a critical donated electron concentration, the sulfur atoms change their coordination around molybdenum from trigonal prismatic to octahedral, thus forming 1T'-MoS₂.^{28–31} Constructing heterointerfaces by interfacing MoS₂ with other two dimensional (2D) materials could modulate the charge donation from lithium at the heterointerface, thus enabling the study of nucleation pathways in the lithium-induced 2H-1T' phase transition of MoS₂. Recently, heterointerface effects in the electrochemical intercalation of van der Waals (vdW) heterostructures have been investigated to understand how heterointerfaces modulate electron transport and lithium storage.³² However, heterointerface effects on the phase transition, and consequently on the nucleation pathway, have not been examined.

We investigate the effects of a heterointerface on the phase transition of MoS₂ by considering the lithium intercalation of two heterostructures: graphene-MoS₂ and hexagonal boron nitride (*h*BN)-MoS₂. Upon lithium intercalation, graphene readily accepts charge from lithium,^{33,34} while insulating *h*BN is not expected to interact significantly with intercalated lithium.^{35,36} We employed density functional theory (DFT) calculations to determine the equilibrium configuration of the graphene-MoS₂ and *h*BN-MoS₂ heterointerfaces with a Li intercalant, followed by Bader charge analysis to determine how charge from the Li is donated at each heterointerface. As shown in Figure 1, Li donates close to 1 electron to freestanding MoS₂. Consistent with our previous work,³⁶ the amount of charge donated by Li is slightly reduced at the *h*BN-MoS₂ heterointerface, with 90% of the charge donated to the MoS₂ layer and 10% donated to the *h*BN. At the graphene-MoS₂ heterointerface, however, we find a dramatic reduction in charge donation from Li to MoS₂, with 34% of the charge transferred to the MoS₂ layer and 48% to the three adjacent graphene layers (the rest of the charge (18%) is donated to the bottom three graphene layers (now shown in the schematic in Fig. 1b)). Density of state calculations show that lithium can dope electrons across a wide range of energies at the MoS₂-graphene heterointerface (Supplementary Fig. 1). Thus, we find that interfacing MoS₂ with graphene lowers the overall charge donated, and hence the effective doping power of Li, to MoS₂ by ~60% when compared to both the MoS₂-*h*BN heterostructure and freestanding MoS₂.

Motivated by the DFT analysis, we fabricated heterostructures of several-layer MoS₂ interfaced with graphene and *h*BN using mechanically exfoliated microflakes patterned with Cr/Au electrical contacts and supported on SiO₂/Si substrates. These devices were integrated into electrochemical microreactors,^{32,34,36–38} in which the Cr/Au-contacted heterostructures served as the working electrode, while lithium metal pressed onto copper foil served as the counter electrode

(Supplementary Fig. 2). These electrodes were immersed in a liquid electrolyte (LiPF_6 in EC/DEC) and sealed in an airtight cell fitted with a glass window to allow for *in situ* optical and Raman characterization during intercalation. Intercalation was controlled potentiostatically by sweeping the electrochemical potential (V_{EC}) between the working electrode and lithium metal. As V_{EC} was sequentially lowered from open circuit voltage (OCV, ~ 2.5 V vs. Li/Li^+) to 0.2 V vs. Li/Li^+ at a decrement of 0.2 V, Li^+ ions diffused through the electrolyte and intercalated into the interlayer gaps of the heterostructures. At each potential, V_{EC} was held constant to acquire Raman spectra and optical micrographs *in situ*.

To investigate the effect of a heterointerface between MoS_2 and graphene, we partially covered a MoS_2 flake with graphene to create bare and graphene-covered regions of MoS_2 (Fig. 2a,b). V_{EC} was lowered from OCV to 1.0 V vs. Li/Li^+ , which is the potential at which the 2H-1T' phase transition is expected to occur for bare MoS_2 .³⁶⁻³⁸ *In situ* optical microscopy revealed that the uncovered portion of MoS_2 began to darken at 1.0 V vs. Li/Li^+ (Fig. 2c), indicative of the 2H-1T' phase transition.^{36,38} After 120 minutes at 1.0 V vs. Li/Li^+ , the bare region of MoS_2 completely darkened. Strikingly, the graphene-covered region retained its original blue color even after 120 minutes at 1.0 V vs. Li/Li^+ (Fig. 2c), suggesting that the graphene-covered MoS_2 remained in the 2H phase. *In situ* Raman spectra confirm that the uncovered region of the MoS_2 flake underwent a phase transition at 1.0 V vs. Li/Li^+ as evidenced by the disappearance of the E_{2g} and A_{1g} modes of 2H- MoS_2 and the concurrent growth of the J_1 and J_2 modes of 1T'- MoS_2 (Fig. 2d).^{23,39} By contrast, *in situ* Raman spectra confirm that the graphene-covered region remained in the 2H phase after 120 minutes at 1.0 V vs. Li/Li^+ (Fig. 2e). As V_{EC} was further lowered to 0.9 V, 0.8 V, and 0.6 V vs. Li/Li^+ , the darkened region expanded inwards from the bare region to the graphene-covered region of MoS_2 . However, the growth of the darkened region was slow, and after 20 minutes at 0.6

V vs. Li/Li⁺, only half of the graphene-covered region had undergone the phase transition. At 0.4 V vs. Li/Li⁺, the graphene-covered MoS₂ completed the phase transition to 1T', while the bare region of MoS₂ was fully converted to Mo and Li₂S.^{37,40} For the graphene-covered region, the irreversible conversion reaction occurred at 0.2 V vs. Li/Li⁺. Thus, Figure 2 shows that the graphene-MoS₂ heterointerface significantly delayed the phase transition.

Analysis of *in situ* optical micrographs elucidates the heterointerface effects on the growth dynamics of the 1T' domain (Supplementary Fig. 3). At 1.0 V vs. Li/Li⁺, the bare region of MoS₂ darkened quickly inwards from the flake edges in contact with the electrolyte, suggesting nucleation of 1T' domains at the edges, followed by fast growth of the 1T' domains (Fig. 2f-i and 2f-ii). At 0.6 V vs. Li/Li⁺, the growth of the dark region in the graphene-covered portion of the flake continues slowly from the uncovered region. Thus, when $1.0 \text{ V} > V_{\text{EC}} > 0.4 \text{ V}$ vs. Li/Li⁺, 1T' domains do not nucleate in the graphene-covered region, while growth of already-nucleated 1T' domains is extremely slow (Fig. 2f-iii). At 0.4 V vs. Li/Li⁺, the growth of the 1T' domain accelerated significantly and also proceeded from the graphene-covered edges inwards (Fig. 2f-iv), until the entire covered-region of MoS₂ fully converted to the 1T' phase (Supplementary Fig. 3). The graphene-MoS₂ heterointerface effects on the phase transition of MoS₂ were reproduced in a replicate device (Supplementary Fig. 4). We note that *in situ* Raman spectroscopy is sufficient to study these phase transitions as Raman spectra for the 2H and 1T' phases are distinct. *In situ* x-ray diffraction would produce too little signal for the microflakes under study, while *in situ* transmission electron microscopy is challenging with liquid electrochemistry.

From these experiments, we conclude that the 2H-1T' phase transition initiates via heterogenous nucleation. Our *ab initio* calculations show the electron doping power of lithium to MoS₂ is reduced at the graphene-MoS₂ heterointerface, suggesting that a greater applied V_{EC} , and

thus a higher lithium concentration, is required to achieve the same donated electron concentration at the graphene-MoS₂ heterointerface. However, only the top-most MoS₂ layer is expected to lose electron density to graphene, leaving the doping power of lithium in the interior vdW gaps of MoS₂ unchanged. Since our flakes are thicker than 5 layers, the heterointerfaced layer represents less than 20 % of the volume. If the nucleation of 1T' phase were homogeneous, i.e., from the interior volume of MoS₂, we would expect a mixed Raman spectrum of both the 2H and 1T' phases; however, we do not observe the coexistence of both phases. Therefore, we conclude that the phase transition must initiate at the heterointerface between graphene and MoS₂. Furthermore, the growth of the 1T' phase must also be heterogeneous, propagating along the heterointerface, rather than through the interior of the flake. At 1.0 V vs. Li/Li⁺, the graphene-covered region of MoS₂ remained in the 2H-phase while the uncovered region fully converted to the 1T' phase, forming a lateral 2H-1T' heterointerface (Fig. 2f-ii). If growth of the 1T' phase progressed homogeneously, then the 1T' phase would be expected to grow from the interior layers at 1.0 V vs. Li/Li⁺ regardless of the heterointerface at the uppermost layer, which we do not observe. This observation is consistent with previous electron diffraction analysis of intercalated bulk MoS₂ using *in situ* TEM, which suggested that the 2H-1T' phase transition front propagated along the top and bottom free surfaces before the interior regions.⁴¹

The nucleation barrier for the 1T' phase can thus be modulated by a heterointerface. To further investigate the heterogeneous nucleation, we fabricated a graphene/MoS₂/graphene heterostructure in which MoS₂ is completely encapsulated by top and bottom graphene flakes with two heterointerfaces (Fig. 3a,b). During the intercalation of lithium into this heterostructure, *in situ* optical microscopy and Raman spectroscopy revealed that the MoS₂ flake remained in the 2H phase even after V_{EC} was lowered to 0.4 V vs. Li/Li⁺ (Fig. 3c,d), an applied voltage at which

pristine MoS₂ breaks down to Mo clusters and Li₂S (Fig. 2d). The 1T' phase was finally nucleated when V_{EC} was lowered to 0.2 V vs. Li/Li⁺, at which point the flake darkened (Fig. 3c) and the J₁ and J₂ peaks of 1T'-MoS₂ appeared (Fig. 3d). The delayed phase transition might be because the MoS₂ flake was not directly exposed to the liquid electrolyte. However, in our previous study, we showed that MoS₂ still underwent the phase transition at 1.0 V vs. Li/Li⁺ despite not being exposed to the electrolyte.³⁶ Further intercalation of this heterostructure was not possible due to the destruction of the electrical contacts from the alloying of gold with lithium at 0.2 V vs. Li/Li⁺.^{42,43} Intercalation of a replicate device showed similar results (Supplementary Fig. 5; lithium intercalation into the graphene flakes is shown in Supplementary Fig 6). Thus, using two differently configured heterostructures (Fig. 2 and Fig. 3), we clearly demonstrated a delay in the phase transition of up to 0.8 V, which we attribute to the heterogeneous nucleation and heterogeneous growth of the 1T' phase.

We next investigated the growth kinetics of the 1T' phase at different heterointerfaces by intercalating a heterostructure of MoS₂ partially supported on graphene and partially on SiO₂ where the top basal plane of MoS₂ was exposed to the electrolyte to initiate the nucleation at the top-most layer (Fig. 4a,b). Surprisingly, the bottom graphene-MoS₂ heterointerface accelerated the phase transition instead of delaying it. *In situ* optical micrographs and Raman spectra shown in Fig. 4c-e reveal that the graphene-supported region of the MoS₂ flake not only underwent the phase transition at 1.0 V vs. Li/Li⁺ as expected due to the free top-most layer of MoS₂, but did so faster than the SiO₂-supported region of MoS₂. The graphene-supported region completed the phase transition after 30 minutes at 1.0 V vs. Li/Li⁺, while the SiO₂-supported region did so after 70 minutes at 1.0 V vs. Li/Li⁺. Both regions underwent the irreversible conversion reaction as expected at 0.4 V vs. Li/Li⁺ (Fig. 4d-e), and we observed the same behavior in a replicate device

(Supplementary Fig. 7). This indicates that the mere presence of a graphene-MoS₂ heterointerface is not sufficient to delay the phase transition.

To understand the faster growth kinetics at a MoS₂-graphene heterointerface at the bottom of the MoS₂ flake, we considered two possibilities. The first is more efficient electron injection into MoS₂ for faster intercalation kinetics as graphene makes superior electrical contact to MoS₂ than gold does due to a reduced Schottky barrier at the interface.^{44,45} Thus, it is possible that the graphene-MoS₂ heterointerface facilitated more efficient electron injection than the gold electrode, allowing for a more rapid phase transition to the 1T' phase. However, intercalation of a MoS₂ flake partially supported on graphene and biased only through MoS₂ showed the same enhancement in the phase transition kinetics, eliminating the possibility of enhanced charge injection (Supplementary Fig. 8). The second possibility is that the graphene support could facilitate the release of mechanical strain induced by the phase transition. The 2H-1T' phase transition induces mechanical strain, which can result in the formation of wrinkles and a buckled microstructure.³⁸ *Post mortem* scanning electron microscopy (SEM) of the MoS₂-graphene heterostructures after intercalation revealed that the formation of wrinkles and buckled microstructures was more apparent on the graphene-supported regions of MoS₂ as compared to the SiO₂-supported regions (Supplementary Fig. 9 and Fig. 10). Therefore, we conclude that the MoS₂-graphene heterointerface can relieve the strain caused by the phase transition more easily than the MoS₂-SiO₂ interface, leading to faster kinetics of the phase transition.

Our *ab initio* calculations suggest that while the graphene-MoS₂ heterointerface will reduce lithium's electron doping power to MoS₂, an *h*BN-MoS₂ interface has little effect on the doping power of lithium. To probe this, we fabricated a heterostructure where MoS₂ was partially covered by *h*BN (Fig. 5a,b), and observed that the *h*BN-covered MoS₂ underwent the phase transition at

1.0 V vs. Li/Li⁺ (Fig. 5c,d and Supplementary Fig. 11a), in agreement with our calculations and our previous findings.³⁶ We also probed the kinetics of the phase transition at the heterointerface by fabricating a heterostructure where MoS₂ was partially supported on *h*BN and partially on SiO₂, with the free top basal plane of MoS₂ exposed to the electrolyte (Fig. 5e,f). Just as in the graphene-supported case, the *h*BN-supported MoS₂ underwent the phase transition more rapidly at 1.0 V vs. Li/Li⁺ than the SiO₂-supported region (Fig. 5g,h and Supplementary Fig. 11b). *Post mortem* SEM of this heterostructure revealed a more pronounced wrinkled microstructure of the *h*BN-supported region as compared to the SiO₂-supported region (Supplementary Fig. 11c-e). Therefore, we show that interfacing MoS₂ with a 2D substrate allows for a more rapid phase transition due to the efficient release of mechanical strain due to weak vdW interactions at the 2D heterointerface.

In summary, our results show that the lithium-induced phase transition in MoS₂ proceeds by heterogeneous nucleation of the 1T' phase at a heterointerface rather than homogeneous nucleation, and the nucleation barrier for the 1T' phase is the highest for the graphene-MoS₂ interface, requiring an increase in V_{EC} as high as 0.8 V more than for free MoS₂ surface. The growth kinetics of the phase transition are also influenced by the heterointerface, where 2D vdW interfaces facilitate faster growth kinetics than MoS₂ supported on SiO₂. Our results thus provide microscopic insight into the nucleation pathways for phase transitions in 2D materials and highlight the importance of heterointerfaces on the onset and propagation of phase transitions. Particularly, as graphene and *h*BN are widely employed as nanoscaled electrodes and passivation layers for many 2D heterostructures, understanding their heterointerfacial effects on phase transition dynamics of the active material is of paramount importance.

Methods

Ab Initio Calculations

Density Functional Theory calculations were carried out using a plane-wave basis set within the Projector Augmented Wave^{46,47} approach using the Quantum Espresso⁴⁸ software package. The $4s$ and $4p$ semi-core states of Mo were included as valence electrons and the exchange-correlation was treated at the Generalized Gradient Approximation (GGA) level of Perdew-Becke-Ernzerhof (PBE).⁴⁹ The vdW interactions were accounted for using Grimme's D3 dispersion correction.⁵⁰ A 4×4 MoS₂- 5×5 graphene supercell was used containing 1 monolayer of MoS₂ and 6 layers of graphene, where the graphene was strained in-plane by $\sim -1.3\%$ to create a commensurate interface, with zero strain in the direction normal to the interface. The kinetic energy cut-off for the plane waves was set to 1040 eV, and a Gamma centered Monkhorst-Pack⁵¹ K-mesh of $8 \times 8 \times 1$ was employed to sample the Brillouin Zone. A Li atom was introduced at the preferred site on top of a Mo atom⁵² and all the atoms in the supercell were relaxed until the total energy converged to within 0.2 meV/atom, and the forces on each atom were smaller than 0.03 eV/Å. Bader charge analysis⁵³ was carried on the relaxed equilibrium configuration to determine the change in the charge distribution induced by Li. For freestanding MoS₂, Li donated $-0.88e$ (where e stands for the elementary charge), while in a graphene/MoS₂ heterostructure, Li donated $-0.30e$ to MoS₂ and $-0.42e$ to the three graphene layers adjacent to Li, and $-0.16e$ to the bottom graphene layers. For the hBN-MoS₂ heterointerface, a 4×4 MoS₂- 5×5 hBN supercell was used containing 1 monolayer of MoS₂ and 6 layers of hBN, where the hBN was strained in-plane by $\sim -1.3\%$ to create a commensurate interface. Further details for the hBN-MoS₂ calculations can be found in our previous work.³⁶ Bader charge analysis revealed that for freestanding MoS₂, Li donated $-0.97e$, while in a hBN/MoS₂ heterostructure, Li donated $-0.87e$ to MoS₂ and $-0.1e$ to hBN.

Device Fabrication

Several-layer MoS₂ (SPI Supplies), graphene (NGS Naturgraphit GmbH), and *h*BN (HQ Graphene) flakes were mechanically exfoliated from bulk crystals onto SiO₂/Si substrates using the scotch-tape method. The substrates were sonicated in acetone and isopropyl alcohol, and treated with O₂ plasma prior to exfoliation. MoS₂ flake thickness was identified via the separation between the E_{2g} and A_{1g} Raman modes^{54,55} measured using a Horiba LabRAM HR Evolution Spectrometer with a 532 nm laser and a 1800 lines/mm diffraction grating (Supplementary Fig. 2). Graphene flake thickness was determined via the ratio of the intensity of the Si Raman peak at 520 cm⁻¹ measured with a 633 nm laser through the flake as compared to the intensity of the Si peak measured directly from the substrate as we previously describe.⁵⁶ Raman analysis shows a low defect density in the graphene flakes (Supplementary Fig. 2). *h*BN flake thickness was estimated using optical microscopy.

Flakes of desired size and thickness were transferred to SiO₂/Si substrates using a KOH-assisted technique, as we describe previously^{36,56}. Briefly, a hemispherical droplet of epoxy (Scotch-Weld, Series DP100Plus) on a glass slide was coated with a layer of polypropylene carbonate (PPC, Sigma Aldrich). Using an optical microscope and a micro-manipulator that holds the glass slide, the epoxy/PPC droplet was positioned above a flake of interest and carefully lowered to contact the flake. A 2M aqueous solution of potassium hydroxide (KOH, Sigma Aldrich) was added to the substrate to etch the top few Å of SiO₂, releasing the flake from the substrate onto the epoxy/PPC droplet. Each flake was released from the glass slide by melting the PPC at 95-100 °C for 5 minutes while contacting a target SiO₂/Si substrate. The PPC was

subsequently dissolved in chloroform overnight. Heterostructures were fabricated by repeating this procedure and using the micro-manipulator and rotational stage to carefully control the placement of the second flake on top of the previously-transferred bottom flake. All MoS₂ flakes used in this study were 5-7 layers thick, all graphene support flakes were 6-10 layers thick, and all graphene flakes covering MoS₂ were 5 layers thick to minimize the attenuation of Raman signal from MoS₂.

For electrochemical lithium intercalation, electrodes were patterned with electron beam lithography (Nabity NPGS, Helios G4 FIB-SEM) and then 10 nm Cr / 100 nm Au was deposited using thermal evaporation (Mbraun EcoVap). For partially-covered MoS₂/graphene devices, electrodes were patterned onto both MoS₂ and graphene; for MoS₂ encapsulated by graphene, electrodes were deposited onto both the top and bottom graphene flakes; and for hBN/MoS₂ heterostructures, electrodes were deposited onto MoS₂ only.

Electrochemical Cell Fabrication

Cr/Au-contacted heterostructures fabricated on SiO₂/Si were attached to a glass slide, and the gold contacts of the devices were wire-bonded to aluminum tape for connection to electrical instrumentation. All subsequent steps were conducted in an argon glovebox. For all experiments, intercalation was conducted with a liquid electrolyte using an enclosed cell that holds the device and electrolyte and is sealed with an optical-grade glass top cover.^{36-38,57} Three sides of the glass top cover were first sealed by epoxy (Scotch-Weld, Series DP100Plus), leaving one side open. After the epoxy cured, a small piece (~3×3 mm) of lithium metal (0.38 mm-thick ribbon, Sigma-Aldrich) was pressed onto copper foil using a mechanical plier to ensure good contact. The lithium/copper foil was then inserted into the open side of the glass top cover. The liquid

electrolyte, a battery-grade solution of 1 M lithium hexafluorophosphate in 50/50 v/v ethylene carbonate / diethyl carbonate (LiPF₆ in EC/DEC, Sigma Aldrich), was added to the cell to submerge the device and lithium metal. The open side was then sealed with epoxy, forming an air-tight seal.

In Situ Raman Characterization During Intercalation

Intercalation cells were connected to a Biological SP300 potentiostat/galvanostat for the electrochemical intercalation of Li⁺. The Cr/Au contacts to the device served as the working electrode, while the lithium/copper served as the reference/counter electrode. In all experiments, working electrodes were connected together to allow for simultaneous intercalation through all working electrodes. Before intercalation, a Raman spectrum was taken at OCV (typical OCV values were 2.6 – 2.9 V vs. Li/Li⁺). Lithium was intercalated into the heterostructures potentiostatically by dropping V_{ec} vs. Li/Li⁺ at a scan rate of 10 mV s⁻¹. Upon reaching a desired V_{ec}, the cell was held at that potential while Raman spectra were collected. For multiple intercalation cycles, cells were allowed to recover to OCV before the next intercalation.

All Raman spectra were taken with a Horiba LabRAM HR Evolution Spectrometer using a 633 nm HeNe laser with an 1800 lines/mm diffraction grating. Before intercalation, all samples were characterized at a laser power of ~3 mW to avoid damage, but after cell fabrication, a laser power of ~7.5 mW was used to increase the signal-to-noise ratio due to scattering by the electrolyte. *In situ* Raman spectra were collected with fifteen 5-second exposures. We note that due to extremely low signal, *h*BN flakes could not be characterized at this Raman power (Supplementary Fig. 2). Raman spectroscopy was used to monitor the phase of intercalated MoS₂ as it is a non-invasive technique that can sample the phase throughout the entire thickness of the

heterostructures with micron-scale spatial resolution. Other characterization techniques such as *in situ* transmission electron microscopy are incompatible with liquid electrolytes, while x-ray diffraction or photoelectron spectroscopy conducted on microflakes yield extremely low signals that prevent meaningful analysis.

Post Mortem Characterizations

Post intercalation, the microreactors were opened using a razor blade to remove the epoxy walls to recover the SiO₂/Si on-chip device. Recovered devices were placed into an isopropyl alcohol wash and dried, and then characterized with optical microscopy and Raman spectroscopy. Structural characterization of devices was carried out with SEM (Helios G4 FIB-SEM) at a tilt angle of both 0° and 40°.

References

1. Sleutel, M. *et al.* Nucleation and growth of a bacterial functional amyloid at single-fiber resolution. *Nat. Chem. Biol.* **13**, 902–908 (2017).
2. Van Driessche, A. E. S. *et al.* Molecular nucleation mechanisms and control strategies for crystal polymorph selection. *Nature* **556**, 89–94 (2018).
3. Schmidt-Cernohorska, M. *et al.* Flagellar microtubule doublet assembly in vitro reveals a regulatory role of tubulin C-terminal tails. *Science* **363**, 285–288 (2019).
4. Daneshvar, K. *et al.* lncRNA DIGIT and BRD3 protein form phase-separated condensates to regulate endoderm differentiation. *Nat. Cell Biol.* **22**, 1211–1222 (2020).
5. Kirkby, J. *et al.* Ion-induced nucleation of pure biogenic particles. *Nature* **533**, 521–526 (2016).
6. Kiselev, A. *et al.* Active sites in heterogeneous ice nucleation—the example of K-rich feldspars. *Science* **355**, 367–371 (2016).
7. Zou, L. *et al.* Dislocation nucleation facilitated by atomic segregation. *Nat. Mater.* **17**, 56–62 (2018).
8. Zhou, J. *et al.* Observing crystal nucleation in four dimensions using atomic electron tomography. *Nature* **570**, 500–503 (2019).
9. Jeon, S. *et al.* Reversible disorder-order transitions in atomic crystal nucleation. *Science* **371**, 498–503 (2021).
10. Loh, N. D. *et al.* Multistep nucleation of nanocrystals in aqueous solution. *Nat. Chem.* **9**, 77–82 (2017).

11. Liu, J. *et al.* Incorporation of clusters within inorganic materials through their addition during nucleation steps. *Nat. Chem.* **11**, 839–845 (2019).
12. Cao, K. *et al.* Atomic mechanism of metal crystal nucleus formation in a single-walled carbon nanotube. *Nat. Chem.* **12**, 921–928 (2020).
13. De Yoreo, J. J. *et al.* Crystallization by particle attachment in synthetic, biogenic, and geologic environments. *Science* **349**, (2015).
14. Yang, H., Kim, S. W., Chhowalla, M. & Lee, Y. H. Structural and quantum-state phase transition in van der Waals layered materials. *Nat. Phys.* **13**, 931–937 (2017).
15. Yoshida, M., Suzuki, R., Zhang, Y., Nakano, M. & Iwasa, Y. Memristive phase switching in two-dimensional 1T-TaS₂ crystals. *Sci. Adv.* **1**, 1–7 (2015).
16. Zhang, F. *et al.* Electric-field induced structural transition in vertical MoTe₂- and Mo_{1-x}W_xTe₂-based resistive memories. *Nat. Mater.* **18**, 55–61 (2019).
17. Zhu, X., Li, D., Liang, X. & Lu, W. D. Ionic modulation and ionic coupling effects in MoS₂ devices for neuromorphic computing. *Nat. Mater.* **18**, 141–148 (2019).
18. Voiry, D. *et al.* Enhanced catalytic activity in strained chemically exfoliated WS₂ nanosheets for hydrogen evolution. *Nat. Mater.* **12**, 850–855 (2013).
19. Lukowski, M. A. *et al.* Enhanced hydrogen evolution catalysis from chemically exfoliated metallic MoS₂ nanosheets. *J. Am. Chem. Soc.* **135**, 10274–10277 (2013).
20. Wang, H. *et al.* Electrochemical tuning of vertically aligned MoS₂ nanofilms and its application in improving hydrogen evolution reaction. *Proc. Natl. Acad. Sci.* **110**, 19701–19706 (2013).

21. Voiry, D. *et al.* The role of electronic coupling between substrate and 2D MoS₂ nanosheets in electrocatalytic production of hydrogen. *Nat. Mater.* **15**, 1003 (2016).
22. Yazdani, S., Yarali, M. & Cha, J. J. Recent progress on in situ characterizations of electrochemically intercalated transition metal dichalcogenides. *Nano Res.* **12**, 2126–2139 (2019).
23. Koppera, R. *et al.* Phase-engineered low-resistance contacts for ultrathin MoS₂ transistors. *Nat. Mater.* **13**, 1128–1134 (2014).
24. Kertesz, M. & Hoffmann, R. Octahedral vs. Trigonal-Prismatic Coordination and Clustering in Transition-Metal Dichalcogenides. *J. Am. Chem. Soc.* **106**, 3453–3460 (1984).
25. Dungey, K. E., Curtis, M. D. & Penner-Hahn, J. E. Structural Characterization and Thermal Stability of MoS₂ Intercalation Compounds. *Chem. Mater.* **10**, 2152–2161 (1998).
26. Wang, L., Xu, Z., Wang, W. & Bai, X. Atomic mechanism of dynamic electrochemical lithiation processes of MoS₂ nanosheets. *J. Am. Chem. Soc.* **136**, 6693–6697 (2014).
27. Wang, C. *et al.* Monolayer atomic crystal molecular superlattices. *Nature* **555**, 231–236 (2018).
28. Dresselhaus, M. S. ed. *Intercalation in Layered Materials*. (Springer Science+Buisness Media LLC, 1986).
29. Eda, G. *et al.* Photoluminescence from chemically exfoliated MoS₂. *Nano Lett.* **11**, 5111–5116 (2011).

30. Chhowalla, M. *et al.* The chemistry of two-dimensional layered transition metal dichalcogenide nanosheets. *Nat. Chem.* **5**, 263–275 (2013).
31. Wan, J. *et al.* Tuning two-dimensional nanomaterials by intercalation: Materials, properties and applications. *Chem. Soc. Rev.* **45**, 6742–6765 (2016).
32. Bediako, D. K. *et al.* Heterointerface effects in the electrointercalation of van der Waals heterostructures. *Nature* **558**, 425–429 (2018).
33. *Graphite Intercalation Compounds I.* (Springer-Verlag, 1990).
34. Kühne, M. *et al.* Ultrafast lithium diffusion in bilayer graphene. *Nat. Nanotechnol.* **12**, 895–900 (2017).
35. Zhao, S. Y. F. *et al.* Controlled Electrochemical Intercalation of Graphene/h-BN van der Waals Heterostructures. *Nano Lett.* **18**, 460–466 (2018).
36. Yazdani, S. *et al.* Heterointerface effects on lithium-induced phase transitions in intercalated MoS₂. *ACS Appl. Mater. Interfaces* **13**, 10603–10611 (2021).
37. Wan, J. *et al.* In situ investigations of Li-MoS₂ with planar batteries. *Adv. Energy Mater.* **5**, 1401742 (2015).
38. Xiong, F. *et al.* Li intercalation in MoS₂: *in situ* observation of its dynamics and tuning optical and electrical properties. *Nano Lett.* **15**, 6777–6784 (2015).
39. Jiménez Sandoval, S., Yang, D., Frindt, R. F. & Irwin, J. C. Raman study and lattice dynamics of single molecular layers of MoS₂. *Phys. Rev. B* **44**, 3955–3962 (1991).
40. Xiao, J. *et al.* Exfoliated MoS₂ nanocomposite as an anode material for lithium ion batteries. *Chem. Mater.* **22**, 4522–4524 (2010).

41. Chen, S. *et al.* Atomic structure and migration dynamics of MoS₂/Li_xMoS₂ interface. *Nano Energy* **48**, 560–568 (2018).
42. Taillades, G., Benjelloun, N., Sarradin, J. & Ribes, M. Metal-based very thin film anodes for lithium ion microbatteries. *Solid State Ionics* **152–153**, 119–124 (2002).
43. Zeng, Z., Liang, W. I., Chu, Y. H. & Zheng, H. In situ TEM study of the Li-Au reaction in an electrochemical liquid cell. *Faraday Discuss.* **176**, 95–107 (2014).
44. Zhou, Y. *et al.* Revealing the Contribution of Individual Factors to Hydrogen Evolution Reaction Catalytic Activity. *Adv. Mater.* **30**, 1706076 (2018).
45. Zhou, Y. *et al.* Unveiling the Interfacial Effects for Enhanced Hydrogen Evolution Reaction on MoS₂/WTe₂ Hybrid Structures. *Small* **15**, 1900078 (2019).
46. Blöchl, P. E. Projector augmented-wave method. *Phys. Rev. B* **50**, 17953–17979 (1994).
47. Dal Corso, A. Pseudopotentials periodic table: From H to Pu. *Comput. Mater. Sci.* **95**, 337–350 (2014).
48. Giannozzi, P. *et al.* QUANTUM ESPRESSO: A modular and open-source software project for quantum simulations of materials. *J. Phys. Condens. Matter* **21**, 395502 (2009).
49. Perdew, J. P., Burke, K. & Ernzerhof, M. Generalized Gradient Approximation Made Simple. *Phys. Rev. Lett.* **78**, 1396–1396 (1996).
50. Grimme, S., Antony, J., Ehrlich, S. & Krieg, H. A consistent and accurate ab initio parametrization of density functional dispersion correction (DFT-D) for the 94 elements H-Pu. *J. Chem. Phys.* **132**, 154104 (2010).
51. Monkhorst, H. J. & Pack, J. D. Special points for Brillouin-zone integrations. *Phys. Rev. B*

- 13**, 5188–5192 (1976).
52. Larson, D. T., Fampiou, I., Kim, G. & Kaxiras, E. Lithium Intercalation in Graphene-MoS₂ Heterostructures. *J. Phys. Chem. C* **122**, 24535–24541 (2018).
 53. Tang, W., Sanville, E. & Henkelman, G. A grid-based Bader analysis algorithm without lattice bias. *J. Phys. Condens. Matter* **21**, 084204 (2009).
 54. Li, S. L. *et al.* Quantitative raman spectrum and reliable thickness identification for atomic layers on insulating substrates. *ACS Nano* **6**, 7381–7388 (2012).
 55. Lee, C. *et al.* Anomalous lattice vibrations of single-and few-layer MoS₂. *ACS Nano* **4**, 2695–700 (2010).
 56. Pondick, J. V. *et al.* The effect of mechanical strain on Lithium staging in graphene. *Adv. Electron. Mater.* **7**, 2000981 (2021).
 57. Zhang, J. *et al.* Reversible and selective ion intercalation through the top surface of few-layer MoS₂. *Nat. Commun.* **9**, 1–9 (2018).

Acknowledgements

J.V.P. was supported by the National Defense Science and Engineering Graduate (NDSEG) Fellowship Program, sponsored by the Air Force Research Laboratory (AFRL), the Office of Naval Research (ONR), and the Army Research Office (ARO). J. J. C. acknowledges support from the National Science Foundation (CAREER #1749742). Device fabrication and characterization was carried out at the Yale West Campus Materials Characterization Core and the Yale West Campus Cleanroom. D.Y.Q. and A.K. acknowledge support from the National

Science Foundation under grant no. DMR 2114081. The calculations used resources of National Energy Research Scientific Computing Center (NERSC), a DOE Office of Science User Facility supported by the Office of Science of the U.S. Department of Energy under contract no. DE-AC02-05CH11231 and the Extreme Science and Engineering Discovery Environment (XSEDE), which is supported by the Office of Science of the U.S. Department of Energy under contract no. DE-AC05-00OR22725. We also thank the Yale Center for Research Computing, specifically the Grace cluster for the computing resources.

Author contributions

J.V.P. and J.J.C. conceived the project. J.V.P. carried out the experiments with assistance from M.W. *Ab initio* calculations were performed by A.K. and D.Y.Q. S.Y. and J.M.W. contributed to the development of experimental methods and characterization techniques. J.V.P. and J.J.C. wrote the manuscript with input from all authors.

Competing interests

The authors declare no competing interests.

Supporting information

Supplementary information is available for this manuscript.

Figures

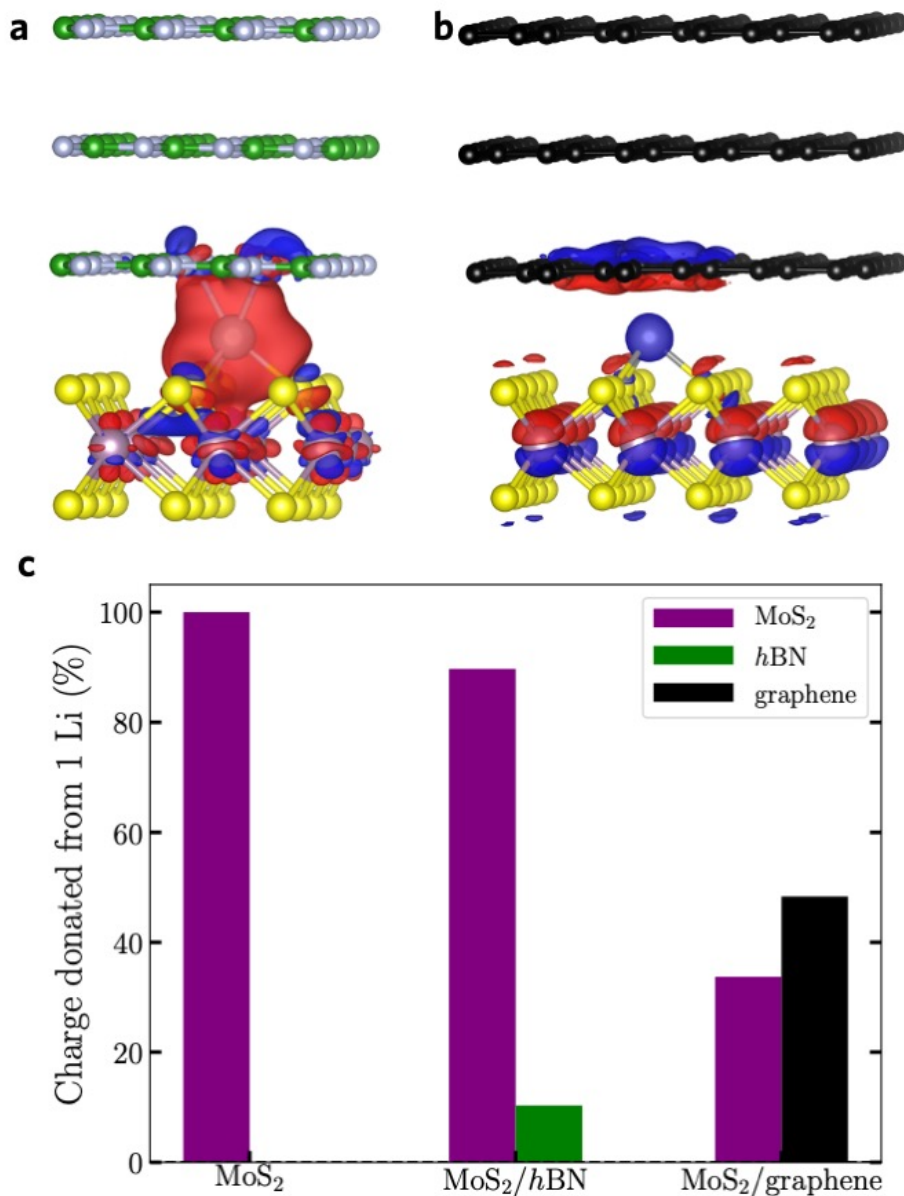


Fig. 1 | Bader charge analysis of MoS₂ heterostructures. a-b, Change in the charge density shown by isosurfaces containing 9% of the maximum charge density with the positive isosurfaces shown in red and the negative isosurfaces shown in blue when Li is introduced in the gap between *hBN* and MoS₂ (a), and the gap between graphene and MoS₂ (b). c, Bader charge analysis showing the percentage of charge donated by the Li to MoS₂ (purple) as well as *hBN* (green) and graphene (black) in the case of freestanding MoS₂ (MoS₂), the *hBN*-MoS₂ heterointerface (MoS₂/*hBN*), and the graphene-MoS₂ heterointerface (MoS₂/graphene).

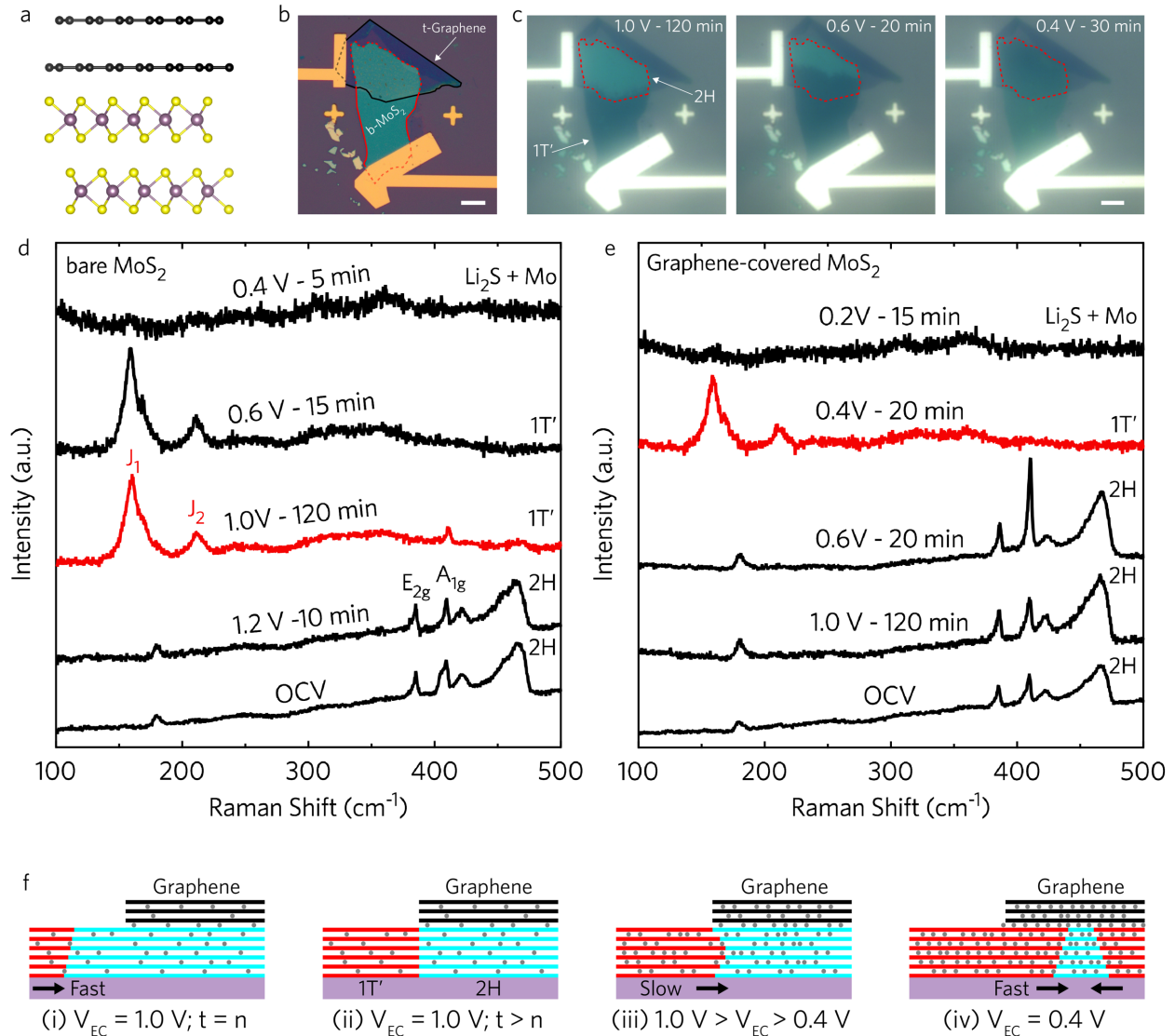


Fig. 2 | Heterointerface-controlled nucleation of the 1T' phase in lithiated MoS₂. **a**, Schematic cross-section of the atomic structure of the graphene-MoS₂ heterointerface. Mo, S, and C atoms are colored purple, yellow, and black, respectively. **b**, Optical micrograph of a MoS₂ flake (red outline) partially covered by a graphene flake (black outline) with gold electrical contacts; scale bar, 10 μm. **c**, *In situ* optical micrographs of the heterostructure in (b) during lithium intercalation at various potentials; scale bar, 10 μm. The dashed-red line outlines graphene-covered MoS₂. The dark color of the bare MoS₂ at 1.0 V vs. Li/Li⁺ is attributed to the 1T' phase, while the graphene-covered region does not completely darken until 0.4 V vs. Li/Li⁺. **d**, *In situ* Raman spectra from the center of the bare region of the MoS₂ flake in the heterostructure in (b) taken during intercalation. The 2H-1T' phase transition (red) is observed at 1.0 V vs. Li/Li⁺, while the conversion reaction is observed at 0.4 V vs. Li/Li⁺. **e**, *In situ* Raman spectra from the center of the graphene-covered region of the MoS₂ flake in the heterostructure in (b) taken during intercalation. The 2H-1T' phase transition (red) is observed at 0.4 V vs. Li/Li⁺, while the conversion reaction is observed at 0.2 V vs. Li/Li⁺. **f**, Schematic cross-section of the heterogeneous nucleation of 1T'-MoS₂ (red) out of 2H-MoS₂ (blue) with arrows indicating the growth direction of the 1T' phase as a function of time (i-ii) and V_{EC} (iii-iv).

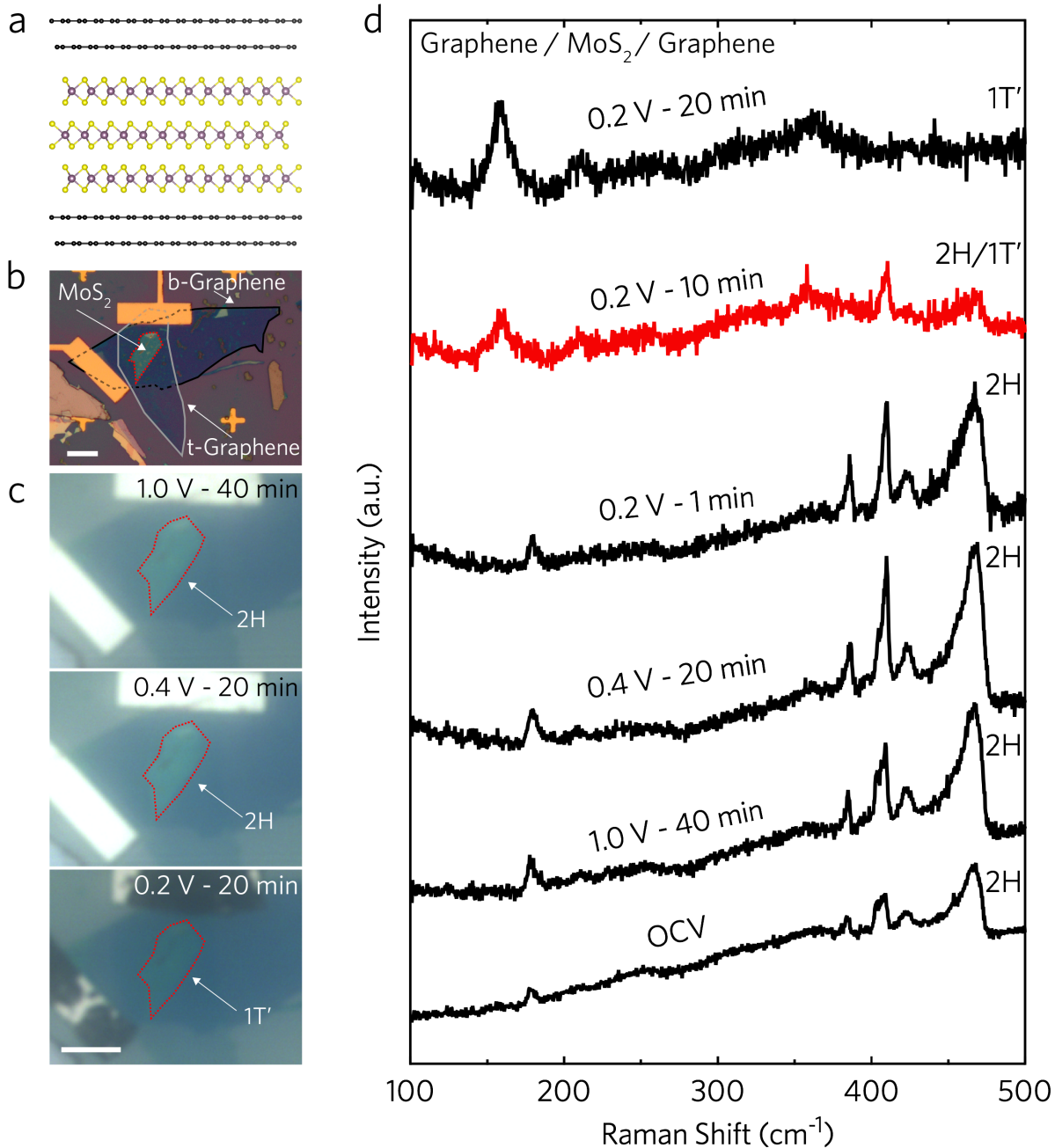


Fig. 3 | Graphene-encapsulation of MoS₂ significantly delays the 2H-1T' phase transition. **a**, Schematic cross-section of the atomic structure of a graphene/MoS₂/graphene heterostructure; Mo, S, and C atoms are colored purple, yellow, and black, respectively. In actual devices, the flakes are several layers thick. **b**, Optical micrograph of a MoS₂ flake (red outline) encapsulated by top (gray outline) and bottom (black outline) graphene flakes with gold electrical contacts; scale bar 10 μm. **c**, *In situ* optical micrographs of the heterostructure in (b) during lithium intercalation; scale bar, 10 μm. The dashed-red line indicates the location of the encapsulated MoS₂ flake. The MoS₂ remains unchanged until 0.2 V vs. Li/Li⁺, at which point it darkens, indicating the onset of the 1T' phase; scale bar 10 μm. The black discoloration of the gold contacts at 0.2 V vs. Li/Li⁺ indicates the alloying of gold with lithium. **d**, *In situ* Raman spectra from the center of the MoS₂ flake in the heterostructure in (b) taken during intercalation. The flake remains in the 2H phase down to 0.4 V vs. Li/Li⁺, and the onset of the 2H-1T' phase transition is observed only after intercalating at 0.2 V vs. Li/Li⁺ for 10 minutes, with the full transition observed after 20 minutes.

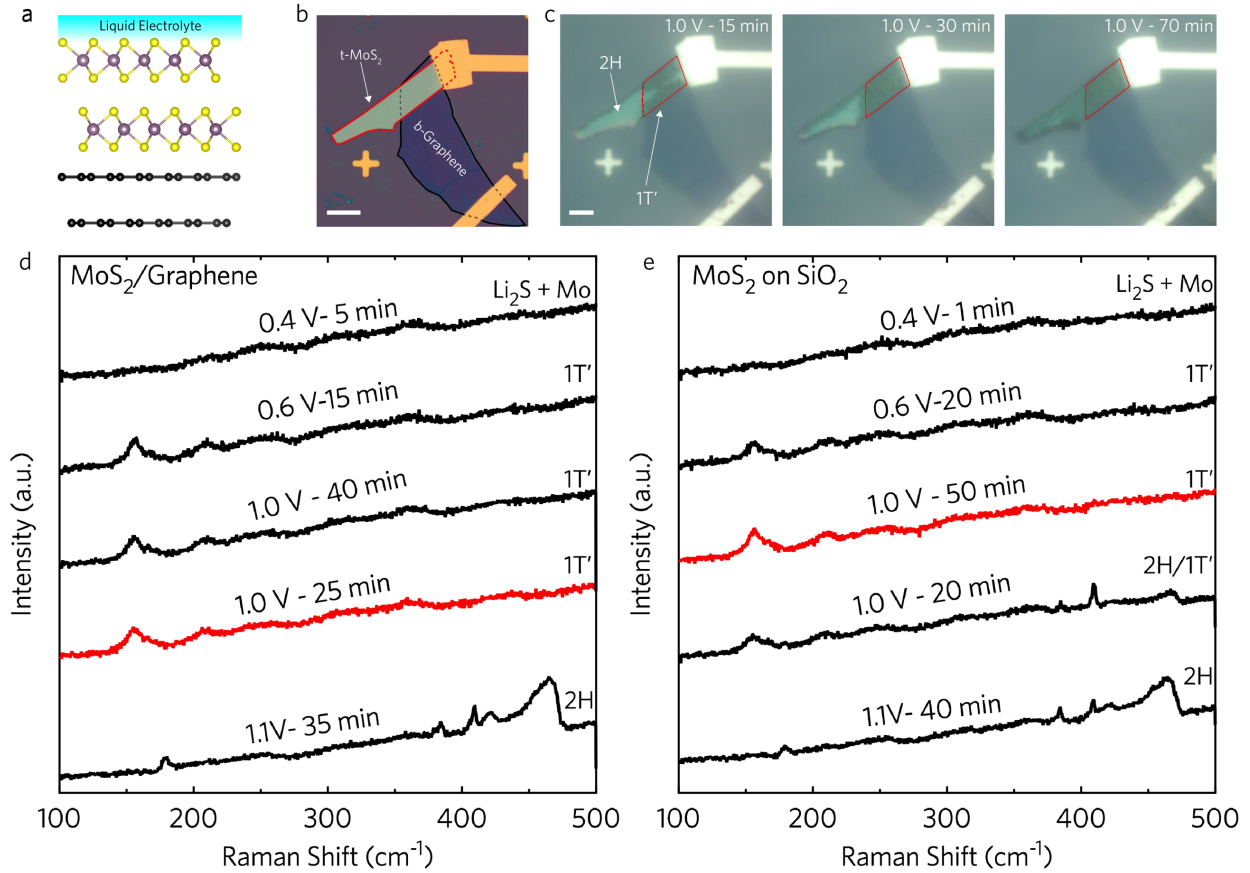


Fig. 4 | Kinetics of the 2H-1T' phase transition in MoS₂. **a**, Schematic cross-section of the atomic structure of a MoS₂/graphene heterointerface where the top basal plane of MoS₂ is in direct contact with liquid electrolyte; Mo, S, and C atoms are colored purple, yellow, and black, respectively. In actual devices, the flakes are several layers thick. **b**, Optical micrograph of a MoS₂ flake (red outline) partially supported on a graphene flake (black outline) with gold electrical contacts; scale bar, 10 μm . **c**, *In situ* optical micrographs of the heterostructure in (b) during lithium intercalation at various potentials; scale bar, 10 μm . The red line outlines the region of the MoS₂ flake supported on graphene. The dark color of MoS₂ at 1.0 V vs. Li/Li⁺ is attributed to the 1T' phase, and the graphene-supported region of MoS₂ completes the phase transition faster than the SiO₂-supported region of MoS₂. **d**, *In situ* Raman spectra from the center of the graphene-supported region of the MoS₂ flake in the heterostructure in (b) taken during intercalation. The 2H-1T' phase transition (red) is observed after 25 minutes at 1.0 V vs. Li/Li⁺, while the conversion reaction is observed at 0.4 V vs. Li/Li⁺. **e**, *In situ* Raman spectra from the center of the SiO₂-supported region of the MoS₂ flake in the heterostructure in (b) taken during intercalation. The 2H-1T' phase transition (red) is observed after 50 minutes at 1.0 V vs. Li/Li⁺, while the conversion reaction is observed at 0.4 V vs. Li/Li⁺.

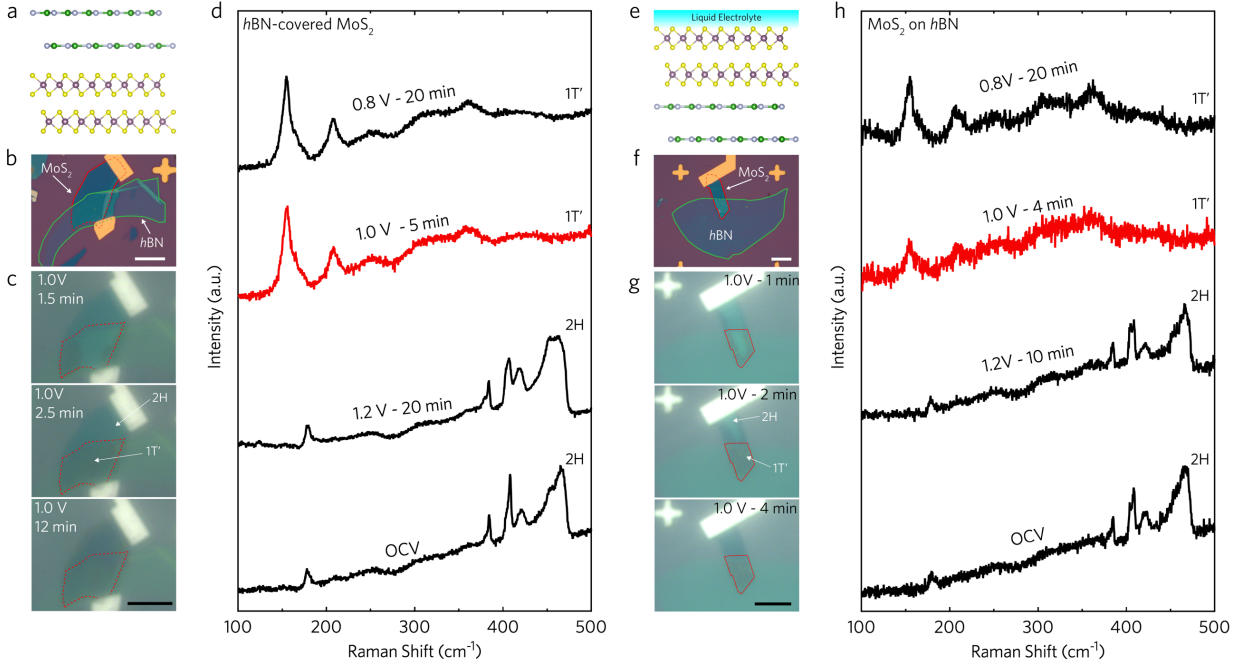


Fig. 5 | Phase dynamics in lithiated MoS₂/hBN heterostructures. **a**, Schematic cross-section of the atomic structure of the hBN/MoS₂ heterointerface with Mo, S, N, and B atoms colored purple, yellow, white, and green, respectively. **b**, Optical micrograph of MoS₂ (red) partially covered by hBN (green) with gold contacts; scale bar, 10 μm. **c**, *In situ* optical micrographs of the heterostructure in **(b)** during lithium intercalation; scale bar, 10 μm. The dashed-red line outlines hBN-covered MoS₂. The darkening of MoS₂ is attributed to the 1T' phase. **d**, *In situ* Raman spectra from the center of the hBN-covered region of MoS₂ in the heterostructure in **(b)** during intercalation. The 1T' phase (red) appears at 1.0 V vs. Li/Li⁺. **e**, Schematic cross-section of the atomic structure of a MoS₂/hBN heterointerface where the top basal plane of MoS₂ is in direct contact with liquid electrolyte; Mo, S, N, and B atoms are colored purple, yellow, white, and green, respectively. In actual devices, the flakes are several-layer thick. **f**, Optical micrograph of MoS₂ (red) partially supported on hBN (green) with gold contacts; scale bar, 10 μm. **g**, *In situ* optical micrographs of the heterostructure in **(f)** during lithium intercalation; scale bar, 10 μm. The red line outlines hBN-supported MoS₂. The darkening of MoS₂ is attributed to the 1T' phase. **h**, *In situ* Raman spectra from the center of the hBN-supported region of MoS₂ in the heterostructure in **(f)** during intercalation. The 1T' phase (red) appears at 1.0 V vs. Li/Li⁺.